UNIVERSITAT DE BARCELONA
Departament d'Astronomia i Meteorologia

UNIVERSITAT DE BARCELONA

Determination of the distance to the Andromeda Galaxy using variable stars

Memòria presentada per
Francesc Vilardell Sallés
per optar al grau de
Doctor en Física

Barcelona, gener de 2009

3 Spectroscopy and spectrophotometry

The second necessary ingredient to fulfill the project goals is the acquisition of spectra. Spectral information is essential because it provides another basic ingredient for distance determination: radial velocities. Therefore, spectroscopy was obtained for five of the 24 EBs selected in Sect. 2.4.1 as suitable candidates for distance determination (Sect. 3.1). Observations were carried out with the Gemini-North telescope and the GMOS detector. The field of view includes four Cepheids, however the S/N and the spectral resolution of the acquired spectra is too low for extracting meaningful information.

Following the procedure used to determine a distance to LMC (Sect. 1.3.2), we obtained spectrophotometry of two of the main targets with the Hubble Space Telescope (HST). Unfortunately, the low quality of the acquired spectra and several technical problems prevented the use of this method to determine the temperature of the components. As shown in Sect. 4.1, the GMOS spectra can also be used to determine the temperature of the components through the fitting of synthetic models. Therefore, the spectrophotometric observations were used to ensure the consistency of the temperature determination (Sect. 3.2).

3.1 Spectroscopy

3.1.1 Observations

The magnitude of the brightest EBs in the photometric catalog is $V \sim 19$ mag. In order to obtain spectroscopy of such objects with the required resolution and S/N for accurate radial velocity determinations a 8–10 m class telescope is required. Considering the position of M 31 in the Northern Hemisphere, we selected the

Table 3.1. Observed targets within the GMOS field of view with the corresponding mean magnitudes and period.

Identifier [M31V]	Var. type	$V^{\rm mean}$ [mag]	$B^{\rm mean}$ [mag]	Reference time [HJD]	Period [days]
J00444528+4128000	EB	18.854 ± 0.021	18.931 ± 0.011	2451814.4644	11.543696
J00442326+4127082	EB	19.242 ± 0.031	19.331 ± 0.021	2452546.4031	5.752609
J00443799+4129236	EB	19.428 ± 0.020	19.348 ± 0.013	2452204.3793	3.549696
J00443610+4129194	EB	20.038 ± 0.031	19.920 ± 0.020	2452908.7081	2.048644
J00445011+4128069	EB	20.456 ± 0.031	20.349 ± 0.011	2452910.5780	2.861049
J00442183+4129492	Cepheid	20.670 ± 0.030	21.391 ± 0.021	2452546.3920	8.246601
J00442951+4130314	Cepheid	21.098 ± 0.035	21.911 ± 0.035	2452546.7483	7.772483
J00444374+4128354	Cepheid	21.499 ± 0.047	22.822 ± 0.068	2452550.7378	14.650850
J00443379+4125219	EB	21.550 ± 0.062	21.333 ± 0.048	2452203.5319	1.739561
J00443928+4130078	Cepheid	21.600 ± 0.068	22.648 ± 0.058	2452906.4932	8.505991

8 m telescope Gemini-North (in Mauna Kea, Hawaii) since it has a multi-object spectrograph (GMOS) that fulfills our requirements.

We used the GMOS spectrograph with a custom mask designed to deliver spectroscopy of a number of targets in a 5′.5 × 5′.5 field of view. The instrument was set to the highest possible resolution of R=3744 ($\sim$ 80km s^{-1} per resolution element) using a slit width of 0″.5. The observations were performed in service mode during four GMOS runs in September, October and November 2004 and February 2005 (program ID GN-2004B-Q-9).

Since the GMOS field of view (5′.5 × 5′.5) is much smaller than the INT photometric field of view (33′.8 × 33′.8), a selection of the optimum area to be studied was performed. Considering the spatial distribution of the EBs selected as suitable candidates for distance determination (see Sect. 2.4.1), a field containing five of the selected EBs at the South-East of the studied region was chosen (Fig. 3.1). Together with the selected binaries, four Cepheids and a fainter EB happen to be within the GMOS field of view (Fig. 3.2) and were also selected for observation (Table 3.1).

The observation strategy consisted in the acquisition of two spectra with an exposure time of 2050 sec. Between the two spectra, a spectroscopic flat-field image and a wavelength calibration arc images were obtained. The two spectra were combined in the data reduction process (Sect. 3.1.2) to produce a combined spectrum. A total amount of eight exposures of 4100 sec and one (obtained in February 2005) with a shorter exposure time (3240 sec) were obtained. All the observations were timed to cover both quadratures of two of the brightest EBs in the field: M31V J00443799+4129236 and M31V J00442326+4127082. The brightest EB (M31V J00444528+4128000) was excluded from the timing constraints because it presents some intrinsic variability and it was estimated (and confirmed afterwards) to be a single-line system from the light curve analysis (Sect. 4.1.3). Therefore, each one of the two main targets has, at least, four observations at

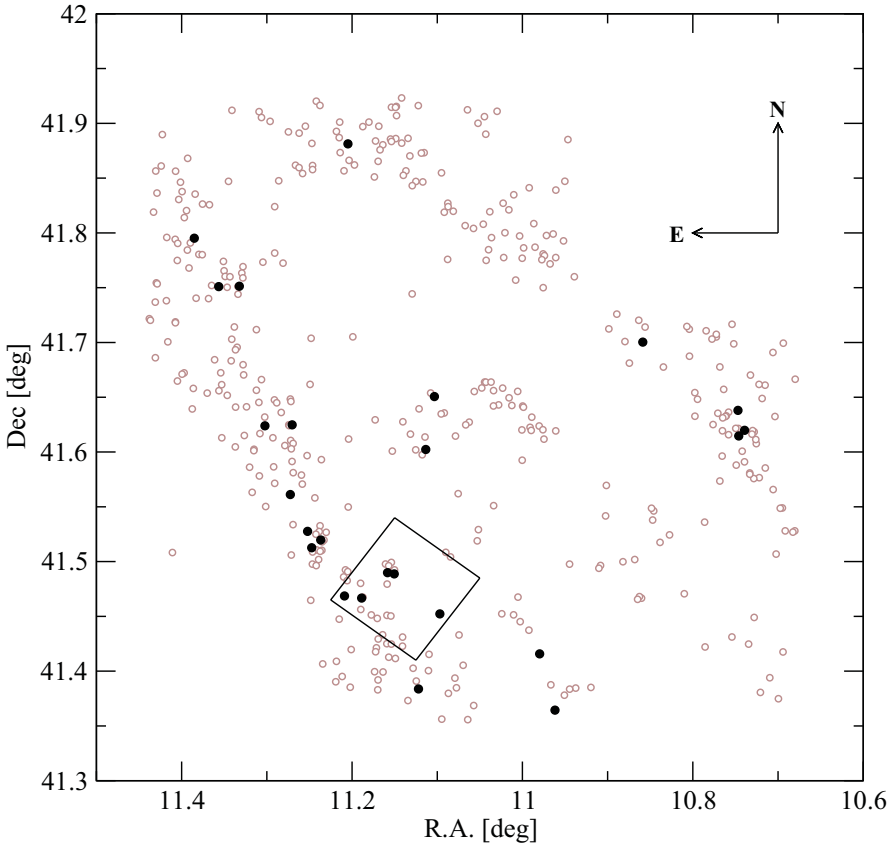

Figure 3.1. Position of the 437 EBs identified in the photometric catalog (gray circles) and the 24 eclipsing binaries most suitable for distance determination (black circles). The area of 5′.5 × 5′.5 selected for Gemini-N/GMOS observations is also indicated (square).

quadratures (two observations per quadrature) and the remaining observations at random phases.

3.1.2 Data reduction

We carried out the reduction of the raw CCD frames with the IRAF Gemini package version 1.7. For each GMOS observing run, several bias (and other calibration data) are automatically obtained out of the scientific program time. From the various possible GMOS configurations, our observations used a binning of 2×2 pixels and the entire field of view was read out. All the bias frames obtained in the same GMOS run, and having the same configuration as the observations, were combined (with a mean and 3σ clipping) to produce a master bias. The corresponding master bias was subtracted from each exposure image.

Before any further corrections could be applied, the position of the spectra in

Figure 3.2. GMOS field of view with the 6 EBs (white circles) and 4 Cepheids (white squares) selected for observation. The white area is the wavefront sensor.

the detector had to be identified. Although the relative position between spectra is known (from the custom mask), the exact position of the spectra on the detector can vary slightly from run to run. Therefore, for each exposure, we first reduced the arc images to derive the displacement of the spectra with respect to the center of the slit.

Once the offsets were known, the wavelength calibration arc and the two spectra in each exposure were flux-corrected with the corresponding flat-field image. Bad pixels and cosmic ray hits were automatically identified (from the neighboring pixels) and each slit was extracted.

Calibration arcs were obtained with a Cu-Ar (Copper-Argon) lamp, providing a wavelength calibration with less than 0.01 nm rms. The wavelength-calibrated spectra were sky subtracted (using the neighboring pixels) and extracted to obtain one dimensional spectra. The across dispersion aperture used to extract each exposure (between 1″and 2″) was found iteratively to obtain the lowest number of bad pixels and the best fit to the spectrum trace. The two one dimensional spectra of each exposure were finally combined (with a mean) and normalized (with a polynomial fit to the continuum), providing the final 4100-second exposures.

With a sampling of about 2.5 pixels per resolution element, all the spectra

Table 3.2. Type of variability, wavelength range, position gaps and signal-to-noise range for each one of the targets observed with GMOS.

Name [M31V]	Type	Range [nm]	Blue gap [nm]	Red gap [nm]	S/N
J00444528+4128000	EB	360.8 – 506.8	408.2 – 409.4	457.4 – 458.5	16 – 30
J00442326+4127082	EB	387.6 – 533.6	435.0 – 436.2	484.2 – 485.3	15 – 35
J00443799+4129236	EB	389.2 – 535.2	436.6 – 437.8	485.8 – 486.9	14 – 39
J00443610+4129194	EB	391.6 – 537.6	439.0 – 440.2	488.2 – 489.3	8 – 24
J00445011+4128069	EB	353.5 – 499.5	400.9 – 402.1	450.1 – 451.2	6 – 12
J00442183+4129492	Cepheid	420.0 – 566.0	467.4 – 468.6	516.6 – 517.7	5 – 12
J00442951+4130314	Cepheid	415.5 – 561.5	462.9 – 464.1	512.1 – 513.2	4 – 9
J00444374+4128354	Cepheid	370.3 – 516.3	417.7 – 418.9	466.9 – 468.0	1 – 6
J00443379+4125219	EB	349.4 – 495.4	396.8 – 398.0	446.0 – 447.1	3 – 6
J00443928+4130078	Cepheid	395.1 – 541.1	442.5 – 443.7	491.7 – 492.8	2 – 6

include the Balmer lines (except Hα at 656.3 nm). The wavelength range was chosen to include Balmer lines because they are almost the only visible (and the strongest) lines for late-O and early-B stars (see Fig. 3.3). Due to the instrument design, the wavelength ranges vary slightly, depending on the position of each EB in the field of view (Table 3.2). In addition, there are two inter-chip gaps in the spectral direction that also vary with the position of each target. For some of the observed targets, one of these gaps happens to be close to the Hβ Balmer line at 486.1 nm.

The spectra obtained (Fig. 3.3) have a S/N ratio that depends on the magnitude of the target and the phase of observation (Table 3.2). Considering the quality of the spectroscopic data acquired, we only selected the five brightest EBs (suitable candidates for distance determination) for further analysis (Chap. 4).

3.2 Spectrophotometry

3.2.1 Observations

Spectrophotometric observations were performed with the Advanced Camera for Surveys (ACS) on board the HST. Two HST orbits were granted in the year 2005 to obtain spectrophotometry of two of the main EBs in the GMOS field of view: M31V J00442326+4127082 and M31V J00443799+4129236. Two ACS detectors were used to observe the desired wavelength interval (from 115 to 1050 nm): the Solar Blind Channel (SBC), with the PR110L prism, and the High Resolution Camera (HRC), with the PR200L prism and the G800L grism (see Table 3.3 for details).

Observations were finally performed in September and November 2006 (Ta-

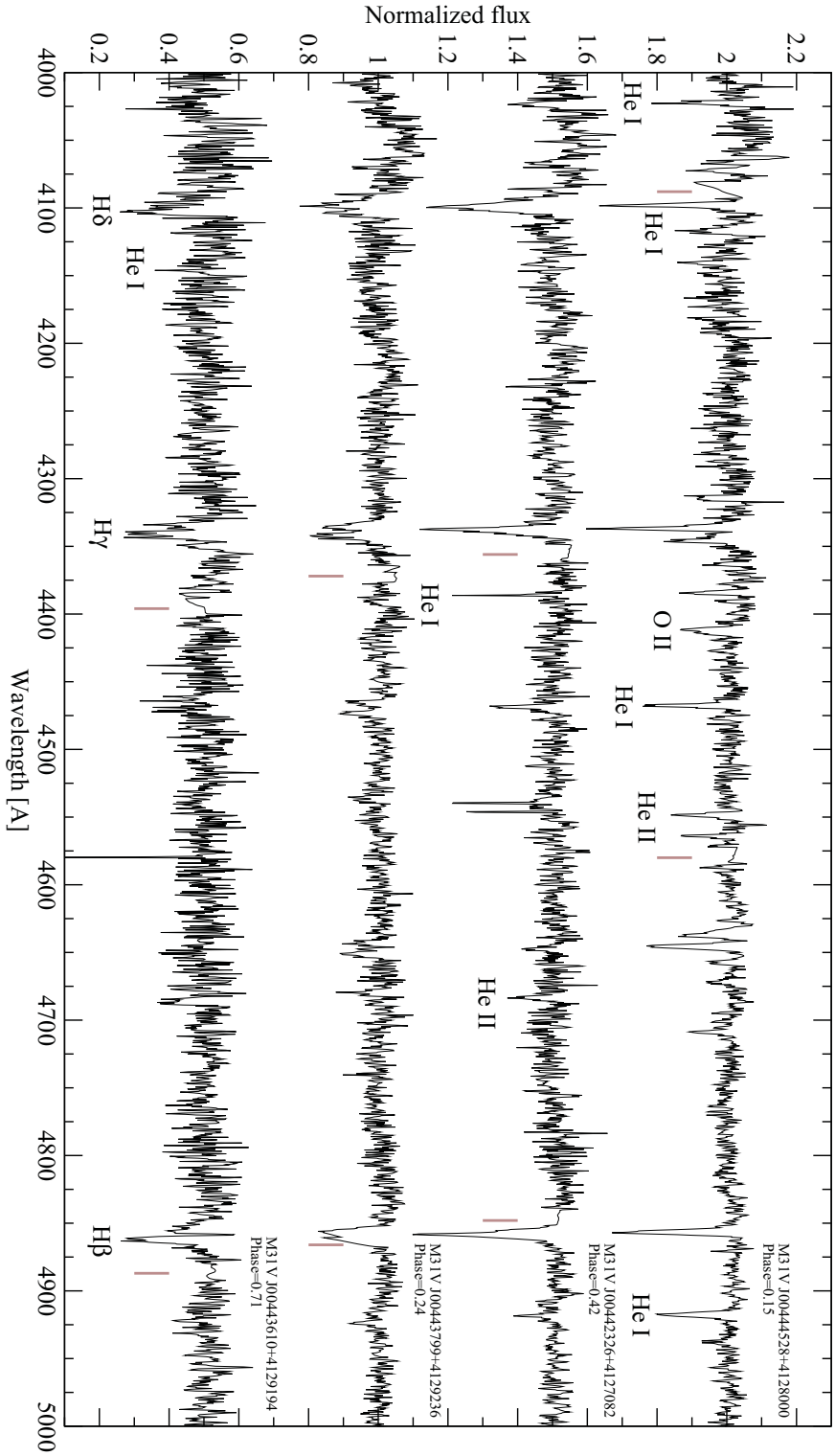

Figure 3.3. Highest quality spectra for the four brightest EBs. The most representative spectral lines are identified, as well as the gaps in the spectra (gray lines).

Table 3.3. Characteristics of the HST instrumentation used to obtain spectrophotometry.

Detector	Field of view	Disperser	Wavelength interval [nm]	Minimum resolution $\lambda/\Delta\lambda$@[nm]	Maximum resolution $\lambda/\Delta\lambda$@[nm]
SBC	$34\farcs6 \times 30\farcs5$	PR110L	115 – 180	40@180	300@115
HRC	29" × 26"	PR200L	170 – 390	13@390	135@170
HRC	29" × 26"	G800L	550 – 1050	70@550	130@1050

Table 3.4. Observations obtained with the ACS camera on board the HST.

Target	Date observed	Orbital phase	Detector	Direct image		Prism/Grism image	
				Filter	Exposure time [seconds]	Disperser	Exposure time [seconds]
[M31V]	[2006]						
J00443799+4129236	September 3	0.77	HRC	F606W	40	G800L	2×117.5
J00443799+4129236	September 3	0.76	HRC	F330W	138	PR200L	2×101
J00443799+4129236	September 17	0.75	SBC	F125LP	113	PR110L	711
J00442326+4127082	November 29	0.56	SBC	F125LP	113	PR110L	711

ble 3.4). Of the two granted targets, only M31V J00443799+4129236 was completely observed, while the other target (M31V J00442326+4127082) was observed only with SBC. Although the underlying reason was never revealed to us, the most likely explanation for the missing data is a failure in ACS, which ceased observations just a few weeks after our run. In addition, although observations were timed to observe both targets at quadratures, the SBC observation of M31V J00442326+4127082 was obtained in the middle of the secondary eclipse (Table 3.4), decreasing the signal of the obtained data and reducing the scientific outcome.

For each spectrophotometric observation a direct image of the selected field of view was obtained (Table 3.4). The obtained data was used in the reduction process (Sect. 3.2.2) to obtain the required zero-points for an accurate wavelength calibration. In addition, for the HRC observations, the spectroscopic data was obtained in two consecutive exposures, enabling the identification and removal of cosmic ray hits. Both exposures were combined in the data reduction process (Sect. 3.2.2).

3.2.2 Data reduction

The data obtained with ACS are automatically processed by the CALACS package. Correction for overscan, bias, darks, flats and some cosmic ray hits is performed. The resulting images were the initial products retrieved from MAST (Multimission Archive Space Telescope science institute) for further analysis. Standard routines in Source Extractor (Bertin & Arnouts, 1996), IRAF (version 2.13.beta) and PyIRAF[1] (version 1.4), including the specific packages for ACS

[1]PyIRAF is a product of the Space Telescope Science Institute, which is operated by AURA for NASA.

data reduction (Multidrizzle and aXe), were used. The reduction procedure is somewhat different for each one of the three different dispersers (HRC G800L, HRC PR200L and SBC PR110L) and, therefore, each procedure is explained separately. In the three cases, calibration and standardization data are provided by the STECF[2] (Space Telescope European Coordination Facility).

3.2.2.1 HRC G800L

The HRC detector is considerably out of the optical axis of HST. Therefore, the obtained images are distorted and had to be corrected (with Multidrizzle). Since two grism images were obtained, the cosmic ray hits were also automatically identified and marked. The lack of contaminating stars in the G800L spectra (present in other images) allowed the application of Multidrizzle with the images obtained just after the CALACS automatic pipeline (either direct images and spectra).

The following step was the identification of the stars in the field. Source Extractor was run on the corrected direct image, identifying the magnitude and position of the EB and nearby companions. Once the stars were identified on the direct image, the spectroscopic images (Fig. 3.4) were background subtracted with a master sky image and bad pixels were automatically identified and removed.

Once the spectra are free from instrumental defects, the extraction of the individual spectra can be performed. The direct image was used to define the reference PSF and zero-point of the wavelength calibration. With the zero-point and the dispersion coefficients provided by STECF, the spectra were wavelength calibrated. The wavelength calibrated spectra were flat fielded (using a wavelength dependent flat field), extracted from the individual exposures and combined to form a single two dimensional spectrum. Each one of the two dimensional spectra was extracted by averaging all the values within 3 times the PSF FWHM and transformed into a one dimensional spectrum. The last step in the reduction of G800L spectra is the transformation of the instrumental flux values into standard ones (using standard calibration data). The applied flux transformations were obtained from two white dwarfs (2MASS J12570233+2201526 and 2MASS J05053062+5249519) and are reported (by STECF) to be accurate to within 5% for all the points between 600 and 900 nm (region between dashed lines in Fig. 3.4).

3.2.2.2 HRC PR200L

The standard procedures in PyIRAF are unable to combine observations obtained in prism mode with HRC. Therefore, considering the lack of atmosphere and the excellent pointing accuracy (with jitters around 6 milliarcsec or 0.2 pixels),

[2]Needed calibration data was obtained from:
`http://www.stecf.org/instruments/ACSgrism/`

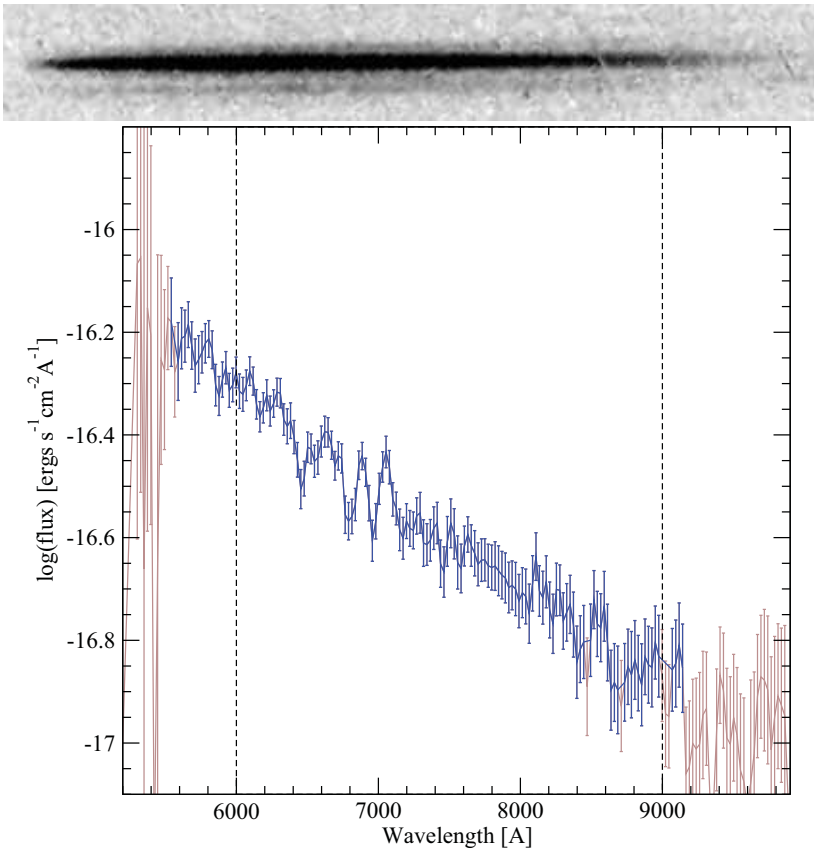

Figure 3.4. Spectroscopic observations obtained with HRC G800L. **Top:** Raw spectrum of M31V J00443799+4129236. **Bottom:** Reduced spectrum (gray lines) with the points having a total error (calibration and random) below 20% indicated (black lines). The area with a calibration error in flux below 5% is also indicated (within the dashed lines).

the pair of HRC prism images were combined (with a weighted mean) after the CALACS automatic procedure and before the correction for image deformation. The combination method is optimal in the sense that the noise is reduced and, at the same time, diminishes the effect of cosmic ray hits.

Unfortunately, the PR200L spectrum of the studied binary is severely contaminated by the presence of a nearby companion (Fig. 3.5). Note that the G800L spectrum is not affected by this contaminating star because the dispersion direction is different. In addition, the contaminating star is much fainter in the optical region, where G800L data was obtained. The instrumental design of the PR200L prism also makes that most of the flux is detected at longer wavelengths and the short wavelength region of the binary spectrum is close to the long wavelength region of the contaminating star, being both equally bright (Fig. 3.5).

In order to avoid negative effects on the extraction of the desired spectrum,

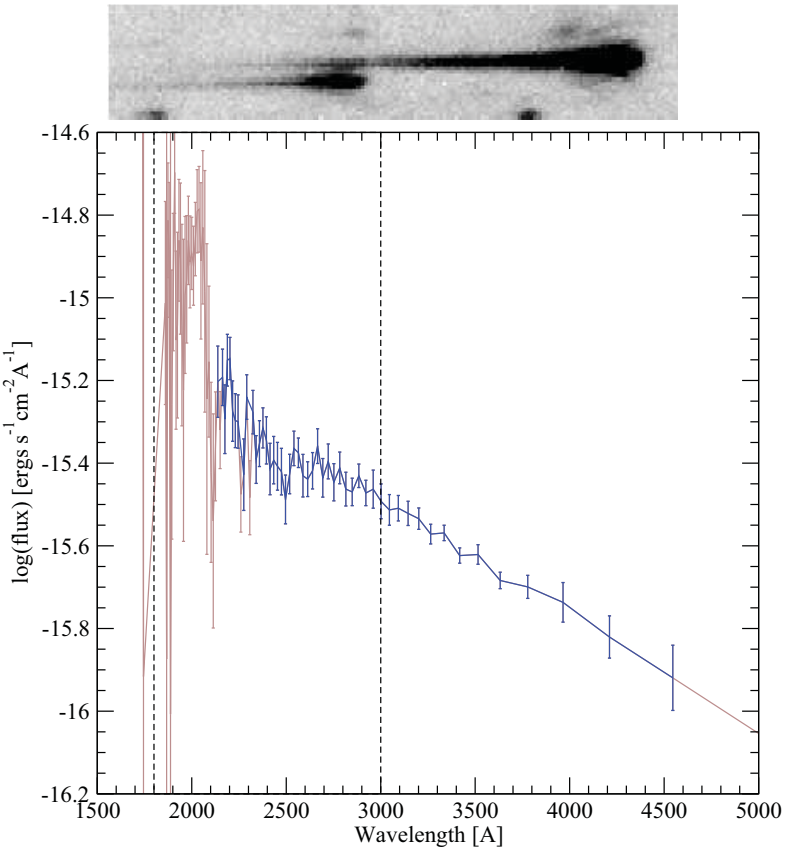

Figure 3.5. Spectroscopic observations obtained with HRC PR200L. **Top:** Raw spectrum of M31V J00443799+4129236. **Bottom:** Reduced spectrum (gray lines) with the points having a total error (calibration and random) below 20% indicated (black lines). The area with a calibration error in flux below 5% is also indicated (within the dashed lines). The effect of contamination is clearly observed at short wavelengths.

the contaminating star was subtracted. Another star in the field of view was used to subtract the contaminating star. In order to ensure that the flux distributions of both stars were similar, the instrumental photometry obtained in the three direct images (with Source Extractor) was used to select the most suitable star. Even when the contaminating star was subtracted, the spectral region affected by contamination was unsuitable for flux determination, but this process ensured that the extraction direction of the spectrum of the EB (automatically detected for the extraction algorithm) is accurate.

Once the binary spectrum was cleaned from contamination, the PR200L data reduction was similar to that used for G800L. The geometric distortions were corrected (with Multidrizzle) and the stars in the field were identified (with Source Extractor). Contrary to the G800L reduction, each individual spectrum was background subtracted from the neighboring pixels (with a median) since no master

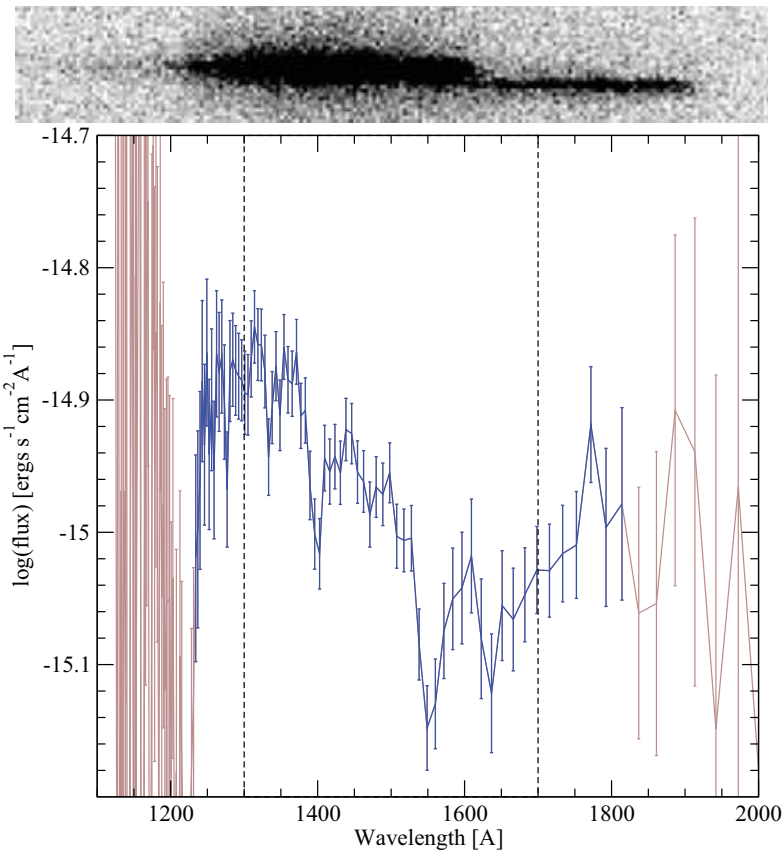

Figure 3.6. Spectroscopic observations obtained with HRC PR110L. **Top:** Raw spectrum of M31V J00443799+4129236. **Bottom:** Reduced spectrum (gray lines) with the points having a total error (calibration and random) below 20% indicated (black lines). The area with a calibration error in flux below 5% is also indicated (within the dashed lines).

sky image is available. The background-subtracted spectra were finally extracted (with an aperture of 0.″5), transformed into one dimensional data, wavelength calibrated and converted to flux standard values using standard calibration data. The applied flux transformations are reported (by STECF) to be accurate within 5% from 180 to 350 nm, but the contaminating star makes that errors larger than 20% are obtained for wavelengths shorter than 215 nm (Fig. 3.5).

3.2.2.3 SBC PR110L

The data reduction process of both targets observed with the SBC detector followed similar steps. The only exception is the treatment of contamination for the M31V J00443799+4129236 data. Contrary to HRC PR200L data, the spectrum of the observed EB is only slightly affected by the contaminating star (Fig. 3.6).

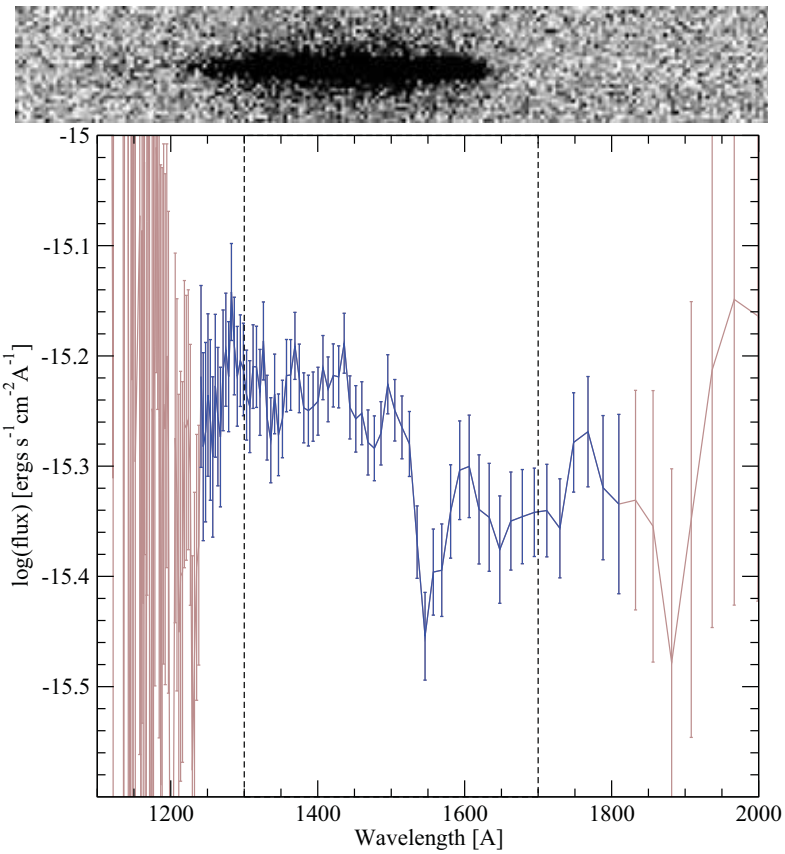

Figure 3.7. Spectroscopic observations obtained with HRC PR110L. **Top:** Raw spectrum of M31V J00442326+4127082. **Bottom:** Reduced spectrum (gray lines) with the points having a total error (calibration and random) below 20% indicated (black lines). The area with a calibration error in flux below 5% is also indicated (within the dashed lines).

Therefore, the subtraction procedure (described for the PR200L data) provided a clean spectrum where the contamination from the nearby companion is well within the observational errors.

For both targets the geometric distortions were corrected (with Multidrizzle) and the stars in the field were identified (with Source Extractor). Contrary to previous reductions, an offset had to be applied to the obtained position of stars in order to use the standard wavelength calibration coefficients. The reason is that coefficients are valid for images taken with the F165LP filter, whereas our direct images were obtained with the F125LP filter. According to the STECF guidelines[3], the required offset in the position of stars is 0.97 pixels in the along dispersion direction and −2.44 pixels in the across dispersion direction. After

[3] Offsets are available at:
`http://www.stecf.org/instruments/ACSgrism/calibration/sbc_pr110l.php`

careful examination of the resulting spectra, it was concluded that the SiIV line at 140 nm and the CIV line at 155 nm were displaced by ∼1 pixel. On the contrary, after the application of the recommended across dispersion offset, it was observed that the extracted spectrum was well centered in the extraction zone. Therefore, no offset in the along dispersion direction was applied and the recommended offset in the across dispersion direction was used.

Once the observed stars were properly identified in the field, the spectra were background subtracted (from the neighboring pixels), and transformed into one-dimensional spectra with an aperture of 0.″5. The observations were finally transformed into flux values with the standard calibration data (Fig. 3.6 and Fig. 3.7). The applied flux transformation is reported (by STECF) to be accurate within 5% for all the values between 130 nm and 170 nm.